

> REPLACE THIS LINE WITH YOUR PAPER IDENTIFICATION NUMBER (DOUBLE-CLICK HERE TO EDIT) <

Long-wave infrared sub-monolayer quantum dot quantum cascade photodetector

Zhijian Shen, Zhuo Deng, Xuyi Zhao, Jian Huang, Lu Yao, Xinbo Zou, Chunfang Cao, Qian Gong and Baile Chen

Abstract—In this paper, a long-wave infrared InAs/GaAs sub-monolayer quantum dot quantum cascade photodetector (SML QD-QCD) grown on GaAs substrate is demonstrated. Temperature- and excitation-dependent photoluminescence measurements are used to study the optical properties of the quantum dot active region, which reveal energetically hybrid ground states between the InAs quantum dot and InGaAs quantum well due to the possible inter-mixing of In and Ga atoms during growth process. The device covers a spectral region from 6.5 to 9 μm . At 77 K, a peak responsivity of 7.5 mA/W is found at 8.3 μm (0 V), and a zero-bias differential-resistance-area (R_0A) product of 9008 $\Omega\cdot\text{cm}^2$ is obtained. The white noise-limited detectivity is $6.5\times 10^9 \text{ cm}\cdot\text{Hz}^{1/2}/\text{W}$. These results encourage the SML QD-QCD as a strong competitor for long-wave infrared imaging applications that require normal incidence and low power dissipation.

Index Terms—Long-wave infrared photodetector, sub-monolayer quantum dot, quantum cascade photodetector, GaAs substrate, photoluminescence.

I. INTRODUCTION

LONG-WAVE infrared (LWIR) photodetectors have attracted great interests in numerous applications, including chemical sensing, target imaging, environment and atmosphere monitoring and medical diagnostics [1-4]. The demand for device performance such as detection sensitivity, dark current and operating temperature promotes research on new materials and structures. Among various structures, inter-subband photodetectors based on quantum wells and quantum dots have been rapidly developed in the past few decades since they cover the LWIR spectral range and have a high flexibility

This work was supported in part by the National Key Research and Development Program of China under Grant 2018YFB2201000, in part by the ShanghaiTech University startup funding under Grant F-0203-16-002, in part by the National Natural Science Foundation of China under Grant 61975121, in part by the Strategic Priority Research Program of Chinese Academy of Sciences under Grant XDA18010000; (*Zhijian Shen, Zhuo Deng and Xuyi Zhao contributed equally to this work.*) (*Corresponding authors: Baile Chen, Qian Gong*)

Z. Shen, L. Yao are with School of Information Science and Technology, ShanghaiTech University, Shanghai 201210, China, with the Shanghai Institute of Microsystem and Information Technology, Chinese Academy of Sciences, Shanghai 200050, China, and also with the University of Chinese Academy of Sciences, Beijing 100049, China (e-mail: shenzhj1@shanghaitech.edu.cn, yaolu@shanghaitech.edu.cn).

Z. Deng, J. Huang, X. Zou and B. Chen are with School of Information Science and Technology, ShanghaiTech University, Shanghai 201210, China (e-mail: dengzhuo@shanghaitech.edu.cn, huangjian@shanghaitech.edu.cn, zouxb@shanghaitech.edu.cn, chenbl@shanghaitech.edu.cn).

X. Zhao, C. Cao, Q. Gong are with the Shanghai Institute of Microsystem and Information Technology (SIMIT), Shanghai 200050, China (e-mail: xyzhao@mail.sim.ac.cn, ccf@mail.sim.ac.cn, qgong@mail.sim.ac.cn)

for adjusting their operational wavelength.

Enlightened by quantum cascade lasers (QCLs), a new type of inter-subband photodetectors called quantum cascade detectors (QCDs) have been proposed and studied extensively [5-7]. The photocurrent extraction in these devices are based on spontaneous phonon-assisted carrier relaxation over cascade stages, which provides several advantages such as zero-bias operation and low dark current noise. Initially, research on LWIR QCDs have been focused on the direct incorporation of quantum well infrared detector into the quantum cascade configuration, so-called quantum well quantum cascade detector (QW-QCD). For instance, Liu *et al.* reported a QW-QCD with peak wavelength of 14.2 μm at 77 K [8]. Bigioli *et al.* demonstrated a QW-QCD at 9 μm which was embedded into a patch-antenna metamaterial [9]. One common problem for these QW-QCD is that they have no response to normal incident light due to the inter-subband transition selection rules of quantum well, and complex grating structure fabrication is mandatory for efficient light coupling. Recently, the quantum dot (QD) nanostructures have attracted intense interest for optoelectronics devices applications, such as laser, photodetectors, due to the unique three-dimensional confinement of QDs [10-12]. Here, in order to obtain a device which shares the advantages of normal incidence response and zero operational bias of QCD, a new device structure called quantum dot QCD (QD-QCD) which replaces quantum wells with quantum dots as absorption region has recently been demonstrated and reported [13-16]. In some reported QD-QCDs [13, 14], QDs are formed by the Stranski-Krastanov mode. However, in SK QDs, presence of wetting layer can cause problems such as weak carrier confinement and low QD density. In order to address these issues, sub-monolayer (SML) QDs growth mode have been proposed. The smaller dimension of SML QDs over SK QDs offers several benefits, such as higher areal dot density, stronger in-plane confinement of carriers, and no wetting layer required [17]. Most QD-QCD reported so far have been designed for the MWIR spectral range, and devices with high zero-bias detectivity and low dark current have been achieved [13-16]. Nevertheless, very little studies have been focused on QD-QCD based on SML QD operating in the LWIR spectral region.

In this paper, we demonstrate a long-wave infrared QD-QCD based on InAs/GaAs SML QDs grown on GaAs substrate. Optical properties of the QD active region are studied by photoluminescence in detail, and the device optoelectronic characteristics are analyzed and compared with recent LWIR QCD devices.

II. DEVICE DESIGN AND MATERIAL GROWTH

The SML QD-QCD sample was grown on a semi-insulating GaAs (001) substrate by molecular beam epitaxy (MBE). From bottom to top, the structure consists of a 100 nm undoped GaAs

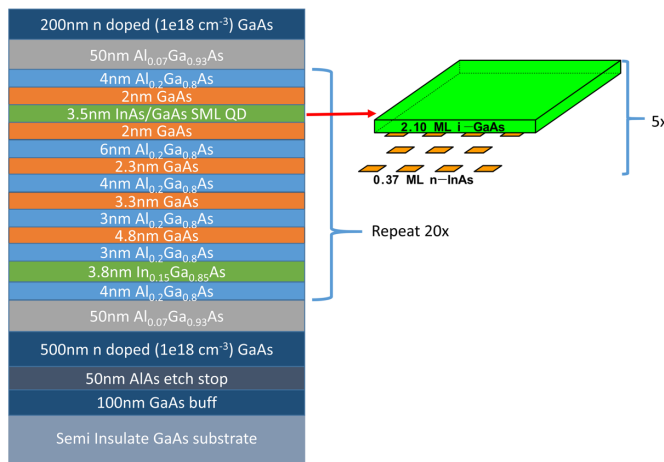


Fig. 1. The schematic diagram of the SML QD-QCD sample structure.

buffer layer, a 50 nm AlAs etch stop layer, a 500 nm GaAs bottom contact layer with Si doping ($n=1 \times 10^{18} \text{ cm}^{-3}$), an active region with 20 periods of quantum cascade structures sandwiched between two 50 nm $\text{Al}_{0.07}\text{Ga}_{0.93}\text{As}$ barriers, and a 200 nm GaAs top contact layer with the same doping as the bottom contact. The role of the two barrier layers grown on both sides of the active region is to suppress the tunneling injection of carriers into the SML-QDs from the contacts [13]. Similar to previous mid-wave infrared SML QD-QCD reports from our group [15, 16], the active region of the sample consists of 5 stacks of SML-QDs (2 electrons/dot) with alternate n -doped InAs (0.37 ML)/undoped GaAs (2.10 ML) deposition, surrounded by 2 nm of GaAs, and a 4 nm $\text{Al}_{0.2}\text{Ga}_{0.8}\text{As}$ confinement enhancing barrier on top. The subsequent QWs are designed to form multiple cascade stages with energy difference of one LO-phonon of GaAs ($\sim 36 \text{ meV}$), enabling efficient extraction of photoexcited electrons. The first three QWs are formed with strain-free $\text{Al}_{0.2}\text{Ga}_{0.8}\text{As}/\text{GaAs}$ with thickness of 6/2.3, 4/3.3 and 3/4.8 nm. The final stage is comprised of a 3 nm $\text{Al}_{0.2}\text{Ga}_{0.8}\text{As}/3.8 \text{ nm In}_{0.15}\text{Ga}_{0.85}\text{As}$ QW. The GaAs buffer, contacts, AlAs etch stop, and $\text{Al}_{0.07}\text{Ga}_{0.93}\text{As}$ blocking layers were grown at 580°C . Subsequently, the substrate temperature was cooled down to 500°C to grow the active and cascade regions. Finally, the temperature of substrate was increased to 580°C again for the growth of the top AlGaAs blocking and GaAs contact layers. Fig. 1 depicts the schematics of sample structure and Fig. 2 shows a single period of the conduction band of the device along with energy level and wavefunction calculated by the one-dimensional k - p model [18-21].

III. MATERIAL OPTICAL CHARACTERIZATION

The optical properties of the SML QD-QCD structure were investigated by using the temperature- and excitation-dependent photoluminescence (PL) techniques. The 532 nm line from a diode laser was collimated and focused on the wafer which was placed in a closed-cycle He cryostat. The PL signal was collected by a gold-plated concave mirror and directed into a Fourier Transform Infrared Spectrometer (FTIR) equipped with an InGaAs detector. Fig. 3 shows the PL spectra of the SML QD-QCD sample measured from 11 to 300 K, with the laser excitation intensity fixed at 25 W/cm^2 . At low temperature

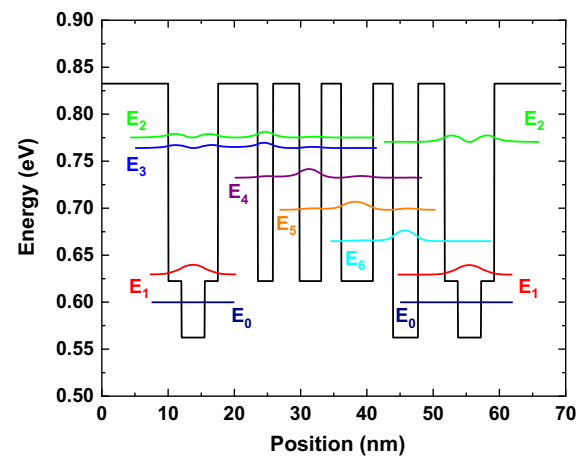


Fig. 2. One period of the conduction band of the device with energy level and wavefunction calculated by the one-dimensional k - p model. Starting from the left, the corresponding layer sequence is: 4 nm $\text{Al}_{0.2}\text{Ga}_{0.8}\text{As}/2 \text{ nm GaAs}/3.5 \text{ nm InGaAs}/2 \text{ nm GaAs}/6 \text{ nm Al}_{0.2}\text{Ga}_{0.8}\text{As}/2.3 \text{ nm GaAs}/4 \text{ nm Al}_{0.2}\text{Ga}_{0.8}\text{As}/3.3 \text{ nm GaAs}/3 \text{ nm Al}_{0.2}\text{Ga}_{0.8}\text{As}/4.8 \text{ nm GaAs}/3 \text{ nm Al}_{0.2}\text{Ga}_{0.8}\text{As}/3.8 \text{ nm In}_{0.15}\text{Ga}_{0.85}\text{As}$. E_0 is the schematic representation of the QDs ground state which is based on semi-empirical estimation from the PL measurement rather than from calculation.

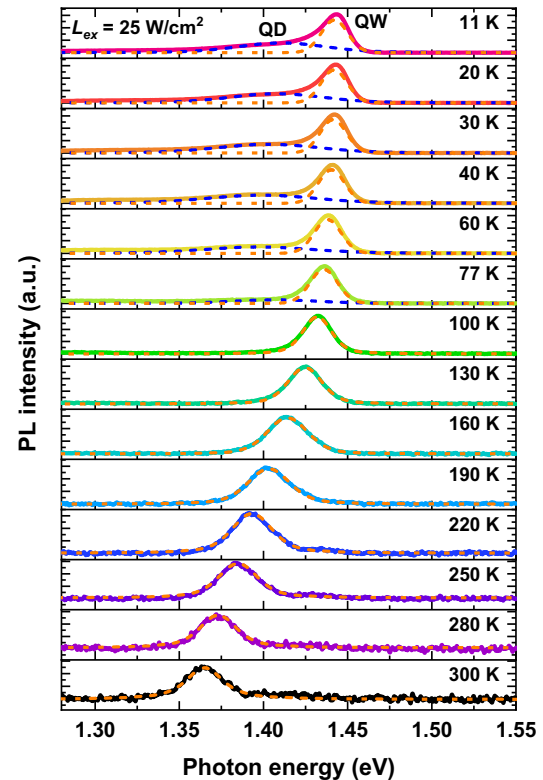


Fig. 3. Temperature-dependent PL spectra of the SML QD-QCD sample measured at laser intensity of 25 W/cm^2 . Fittings of the lineshape are indicated by the dashed curves.

($T < 100 \text{ K}$), the PL emission bands exhibit asymmetric lineshape, indicating multiple recombination mechanisms. In order to gain insights into the electronic band structure, the spectra are calculated by the Voigt model, which combined both Lorentzian and Gaussian broadening factors. It is noted that a good reproduction of the PL band can only be acquired when two emission features are invoked, as shown by the dashed curves in Fig. 3. At 11 K, a dominating emission is

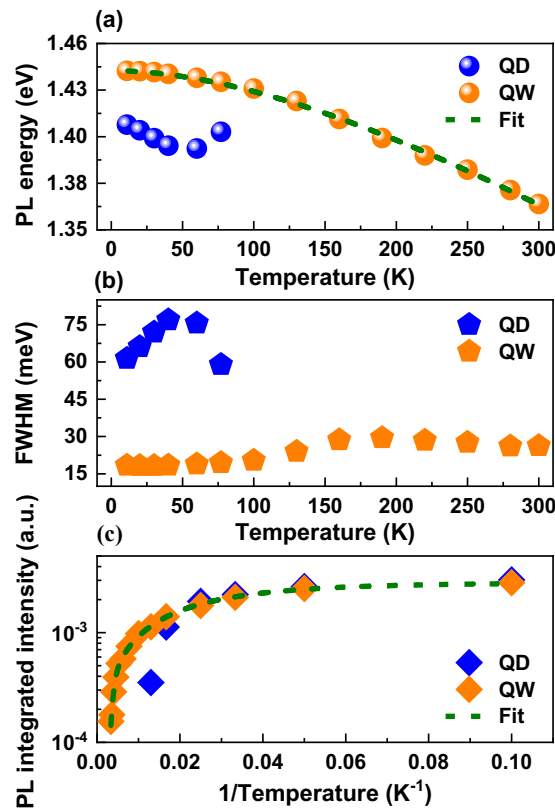


Fig. 4. Temperature dependences of (a) peak energy, (b) FWHM and (c) integrated intensity for both QD and QW emissions extracted from Fig. 3. Solid curves are the fitting results using Eq. (1) and (2), respectively.

observed at 1.442 eV (labeled as QW), and a weaker peak can be resolved at 1.411 eV (labeled as QD). As temperature increases the PL spectra demonstrate typical temperature-induced band-gap redshift. The QD peak quenches rapidly and the emission band is completely dominated by the QW peak from 100 K onward. Meanwhile, the lineshape becomes more symmetric in which only a single peak is needed to generate a good fit. The temperature evolution of PL spectral parameters, i.e., peak position, full-width-at-half-maximum (FWHM) and integrated intensity for both peaks are extracted and plotted in Fig. 4. For the QW emission, the peak energy can be fitted by the empirical Varshni's equation:

$$E_{PL}(T) = E_g(0) - \frac{\alpha T^2}{\beta + T} \quad (1)$$

here, $E_{PL}(T)$ is the PL transition energy, $E_g(0)$ is the band-gap energy at 0 K (11 K in the present case), and α and β are the Varshni's coefficients. The QW peak energy obeys the Varshni's law very well, as can be seen in Fig. 4 (a). The deduced Varshni's coefficient of α and β is 6.1×10^{-4} eV/K and 409.3 K, respectively. However, from Fig. 4 (a) the QD peak energy redshifts much faster and does not follow the Varshni's law. From Fig. 4 (b) the FWHM for both emission peaks increase with temperature, showing a typical PL broadening by the more prominent electron-phonon scattering at higher temperature. Note that the anomalous increase in peak energy and decrease in FWHM at 77 K observed in QD peak are due to uncertainty in fitting. Fig. 4 (c) depicts the integrated intensity of both emission peaks as a function of temperature.

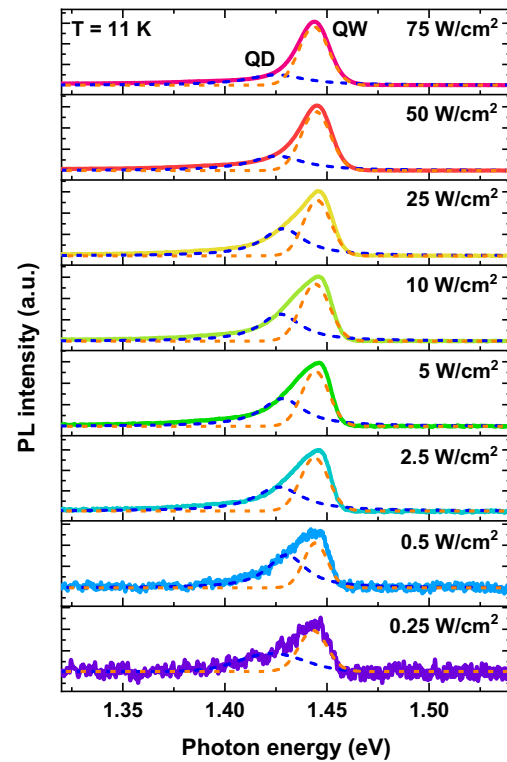


Fig. 5. PL spectra of the SML QD-QW sample measured at different laser excitation intensity at temperature of 11 K. Fittings of the lineshape are indicated by the dashed curves.

In spite of the quick quenching of QD peak, the QW peak can be well observed at room temperature, and its temperature-dependent integrated intensity $I_{PL}(T)$ can be modelled by [22]:

$$I_{PL}(T) = \frac{I_{PL}(0)}{1 + \sum_{i=1}^n a_i T \exp\left(\frac{-E_{ai}}{k_B T}\right)} \quad (2)$$

here, $I_{PL}(0)$ is the PL integrated intensity at 0 K (11 K in the present case), a_i is a coefficient associated with radiative and non-radiative recombination probability, E_{ai} is the activation energy and k_B is the Boltzmann constant. As shown in Fig. 4 (c), for the QW peak the best fit is obtained with two activation routes being considered, i.e., $i=2$ and the two activation energy yields $E_{a1} \sim 2.2$ meV and $E_{a2} \sim 158.9$ meV. E_{a1} is the activation energy responsible for the thermal behavior when T is below 160 K. Its value is comparable to the exciton binding energy of InGaAs quantum well structures [23-25], which suggests that the radiative recombination of the QW PL peak at low temperature regime is excitonic in nature and the intensity quenching is due to the thermal dissociation of exciton into electron-hole pairs. On the other hand, E_{a2} which dominates at temperature above 160 K is in close agreement with the photocurrent peak located at 7.8 μm (~ 158 meV, as shown in Fig. 9). Thus, we believe the rapid quenching of QW emission above 160 K is due to the escape of carriers from the ground state of active region to its excited state ($E_1 \rightarrow E_2$, see Fig. 2).

In order to unmask the origins of the observed emission features, excitation-dependent PL was conducted at 11 K with the laser intensity varied from 0.25 to 75 W/cm², as shown in Fig. 5. Again, the Voigt model is used to calculate the spectral

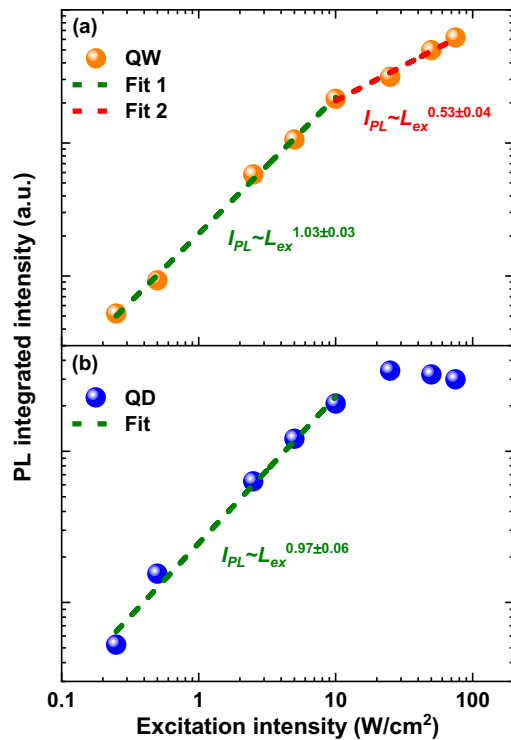


Fig. 6. PL integrated intensity versus excitation intensity for both QD and QW emissions extracted from Fig. 5. The dash lines represent fitting results using Eq. (3).

lineshape and good fits are obtained for all laser intensities with two emission peaks. It is noted that for the variation of laser intensity over two order of magnitude, no obvious shift in peak position and width (FWHM) are seen. This indicates that no heating effect occurs in the sample over the range of laser power employed, and the change of PL intensity is solely correlated to the excitation power. Asymmetric lineshape can be observed from 0.25 W/cm², and gain in integrated intensity is evident in both QD and QW peak as the excitation increases. However, when the intensity is higher than 10 W/cm², the emission from QD peak starts to decline and the asymmetry of PL band alleviates, which indicates a saturation of energy state responsible for radiative recombination of the QD peak. Fig. 6 plots the dependences of PL integrated intensity (I_{PL}) on laser excitation intensity (L_{PL}) for both peaks. The data are modelled by the power law relation [26]:

$$I_{PL} = aL_{PL}^k \quad (3)$$

here a is a coefficient and the exponent k is more crucial since it is indicative of the dominant recombination pathways. In high temperature regime where both radiative and non-radiative recombination mechanism exist, three types of recombination can affect the PL intensity: Shockley-Read-Hall ($k \sim 2$), radiative ($k \sim 1$) and Auger ($k \sim 2/3$) [26]; in low temperature region, non-radiative processes can be negligible and two possible recombination routes are generally considered: free- or bound-exciton ($1 \leq k < 2$) and free-to-bound or donor-acceptor pair ($k < 1$) [27]. As seen from Fig. 6, for the low to moderate laser intensity (< 10 W/cm²) the exponent $k \sim 1.03$ and $k \sim 0.97$ for QW and QD PL peak suggest that the two emissions are most probably associated with the radiative recombination of exciton bound at

electron and hole ground state. This confirms our previous attribution of the QD and QW peak to excitonic recombination in view of its activation energy being comparable to the exciton binding energy of InGaAs quantum wells. Further increase of optical excitation leads to a nonlinear $I_{PL} \sim L_{PL}$ relation for the QW PL peak, as demonstrated by the change in slope of the $\log(I_{PL}) - \log(L_{PL})$ plot. Since the active region of the SML QD-QCD sample is n -doped, and no significant peak shift is observed with increased excitation intensity, we believe the nonlinear change of exponent ($k \sim 0.53$, close to $2/3$) indicates the non-radiative Auger recombination process takes place in the PL transition, possibly due to the increase of photo-generated carrier density under high-injection condition, even at such a low temperature. Hence, based on the behaviors of the QD and QW emission peaks in the above discussion for temperature- and excitation-dependent PL, we consider the QD peak originates from the InAs QD ground state (E_0 in Fig. 2) and the QW peak is from the ground state of the InGaAs QW (E_1 in Fig. 2). This simultaneous transition feature is typically seen in the PL spectra for QDs grown by sub-monolayer technique, which provides direct optical signature of mixed QD and QW states in the InAs/(In)GaAs ensemble. During the growth of SML QDs, alternating short-period InAs/GaAs monolayers were deposited as superlattice, which can theoretically lead to the formation of mini-band for electron and hole states because the thickness of each stack of the InAs/GaAs is within several monolayers. The InGaAs QW (typically with low In content) embedded in the InAs QD matrix could form by the inter-diffusion of In and Ga atoms, either during the deposition of InAs/GaAs superlattice, or during the growth of the top AlGaAs blocking and GaAs contact layers with elevated growth temperature [28]. The resulting energy level scheme of the InAs/(In)GaAs QD ensemble is thus a hybrid QW and QD ground state. Since the SML QDs are intentionally n -doped, the QD ground state can be quickly filled with photo-generated carriers, and the InGaAs QW with higher density of states can dominate the PL band at relatively low excitation intensity, as shown in Fig. 5. The decrease of QD peak intensity when $L_{PL} > 10$ W/cm² is due to the gradual saturation of the QD ground state under high-injection condition. On the other hand, when temperature increases the PL intensity of the QD peak quenches rapidly due to the increased thermal escape probability of carriers from QD states to the QW states. In addition, the inter-dot transfer of photo-excited carriers from smaller QDs to larger QDs can occur via the QW states [28, 29], which can explain the faster temperature redshift of peak energy of the QD band, as observed in Fig. 3 and 4. It is noted that simultaneous QD-QW PL emissions were also reported in conventional QDIP device structure with SML growth mode [30]. This suggests that the effect of atomic intermixing at the InAs/(In)GaAs interface on the electronic structure of active region should be taken into account in device design.

IV. DEVICE FABRICATION AND CHARACTERIZATION

After the optical characterization, the sample was fabricated into a series of mesa-isolated structures with diameters ranging from 20 to 500 μm . Standard UV photolithography and chemical wet etch were used to define the mesas, and e-beam evaporation and lift-off techniques were applied to form the

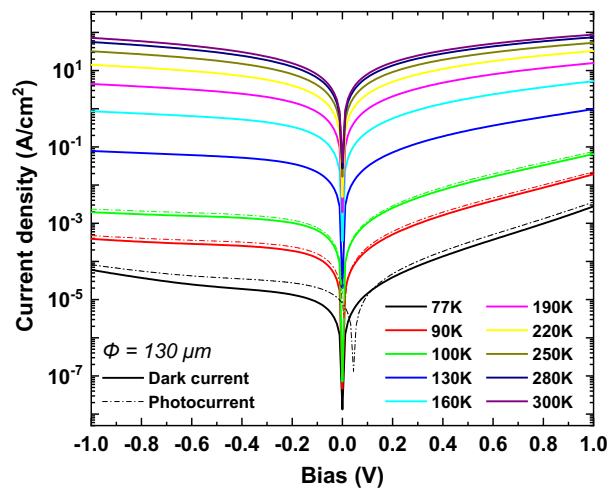


Fig. 7. Current density versus bias voltage for the SML QD-QCD device with 130 μm diameter measured from 77 to 300 K. The solid curves indicate the dark current, while the dash-dotted curves represent the photocurrent.

metal contacts. A SU-8 negative photoresist layer was coated for sidewall passivation. No anti-reflection (AR) coating was applied to the device structure.

Fig. 7 shows the dark current-bias characteristics of a 130 μm diameter SML QD-QCD device measured from 77 to 300 K. During the measurement the sample was loaded in a variable-temperature cryostat cladded with a cold shield and aluminum foil to minimize the background radiation, and the I - V data were collected and analyzed by a semiconductor device analyzer. Photocurrent-bias characteristics measured from 77 K to 100 K are also plotted in Fig. 7. The device photocurrent was measured with the shielding accessories removed from the cryostat and the device was illuminated by a 700 °C blackbody source. As can be seen in Fig. 7, at 77 K the dark current density under zero bias is 1.32×10^{-8} A/cm². On the other hand, the device photocurrent is significantly larger than the dark current, and a positive photovoltaic shift can be observed, demonstrating zero-bias photoresponse of the SML QD-QCD. As the temperature rises, the shift between dark current and photocurrent becomes smaller, and the two curves coincide at 100 K.

Fig. 8 shows the Arrhenius plot of the differential-resistance-area product (R_0A) calculated from the dark current measurement. The R_0A value of the device is $9008 \Omega \cdot \text{cm}^2$ at 77 K and falls to $0.0125 \Omega \cdot \text{cm}^2$ at 300 K. In order to identify the dark current mechanism, the data are fitted by linear function and the activation energy is estimated as $E_a \sim 122.7$ meV. This value is lower than the PL thermal activation energy of QW peak by one GaAs LO-phonon energy (36 meV), which implies that the major leakage path for dark current in this SML QD-QCD device might be the diagonal transition of electrons from the InGaAs QW ground state E_1 to the GaAs/AlGaAs QW cascade level E_4 .

To investigate the optoelectronic characteristics of the QD-QCD device, the device was wire-bonded and loaded into a variable-temperature cryostat for photoresponse measurement. The response was measured in normal incidence configuration by a FTIR spectrometer. A 700 °C blackbody source with modulation frequency of 130 Hz was used to calibrate the responsivity of the detector. The responsivity spectra of the

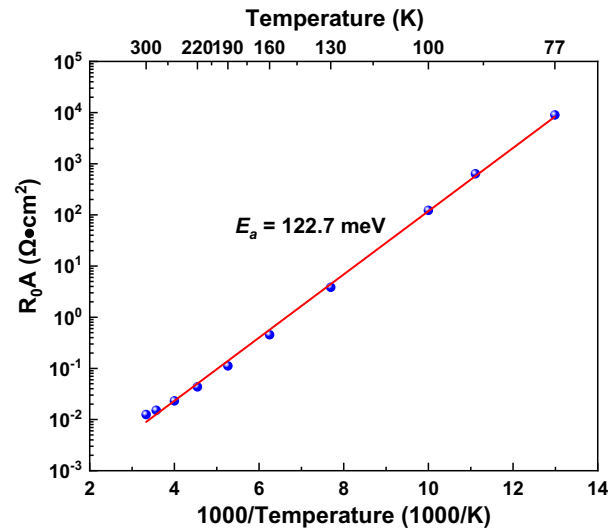


Fig. 8. Arrhenius plot of R_0A product and device temperature.

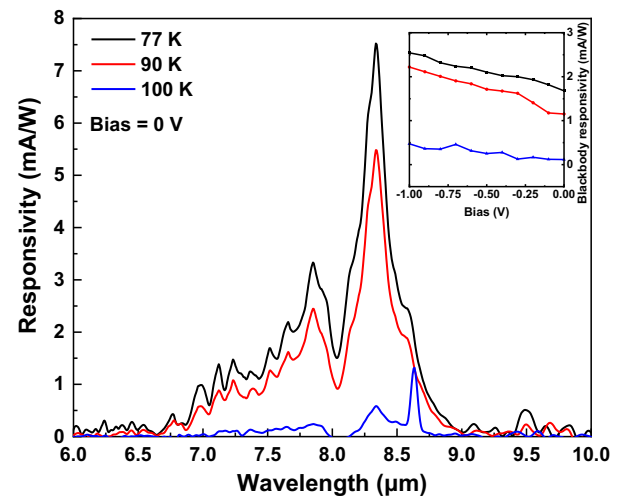


Fig. 9. Normal incident photoresponse of the SML QD-QCD device measured at 77 K, 90 K and 100 K under zero bias. The inset plots the device blackbody responsivity versus bias.

sample measured at 77 K, 90 K and 100 K under zero bias are presented in Fig. 9. The photoresponse covers the spectral range from 6.5 to 9 μm . At 77 K, a peak responsivity of 7.5 mA/W is observed at around 8.3 μm , which corresponds to the inter-subband transition from the InGaAs QW ground state to the first GaAs/AlGaAs QW cascade level ($E_1 \rightarrow E_3$). The peak responsivity drops to 0.6 mA/W when temperature increases to 100 K. It's worth noting that the spectra exhibit a second peak at 7.8 μm , which can be ascribed to the inter-subband transition from the ground state of InGaAs QW to its first excited state ($E_1 \rightarrow E_2$). The stronger response at 8.3 μm could be due to the more efficient relaxation of photo-excited carriers on E_3 compared with those on E_2 . The inset of Fig. 9 shows the blackbody responsivity of the sample as a function of reverse bias. The blackbody responsivity is defined as the ratio between the measured photocurrent and the total incident radiation power from the blackbody source[15]. As the reverse bias increases, the blackbody responsivity increases slightly owing to the fact that larger reverse bias makes the relaxation of electrons in the cascade stages easier.

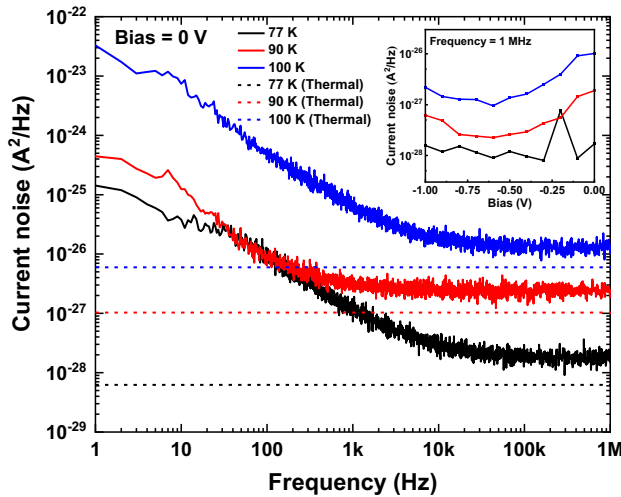


Fig. 10. Current noise power spectral densities as a function of frequency measured from 77 K to 100 K under zero bias (solid curves). The thermal noise calculated by Eq. (4) at corresponding temperature are also shown (dashed lines). The inset shows the dependences of measured noise on reverse bias extracted at 1 MHz.

To evaluate the overall performance of the SML QD-QCD device, current noise of the device was measured at different temperature, as depicted in Fig. 10. The noise data were collected and analyzed by a noise analyzer while the sample was loaded in the cryostat with the same shielding configuration as applied in the dark current measurement. The frequency-independent thermal noise of the device at different temperature are also shown in Fig. 10, given by the formula [14, 15]:

$$\langle i_{thermal}^2 \rangle = \frac{4kT}{R_0} B \quad (4)$$

here R_0 is the differential resistance, k is the Boltzmann constant, T is the temperature and B is the measurement bandwidth. As shown in Fig. 10, the measured current noise curve is higher than the thermal noise at all temperature of interest. In the high frequency flat regime where the device overall noise sources are white noise, the differences between measured data and the calculated thermal noise and shot noise may indicate the existence of other characterization equipment related noise sources. In low frequency region, the measured noise levels are much higher due to the presence of $1/f$ noise and generation/recombination noise. The inset of Fig. 10 plots the dependence of current noise on reverse bias at 1MHz, showing an undulation of the device noise level with increasing reverse bias. Detail analysis on the noise characteristics of this SML QD-QCD device will be the subject of our future work.

Finally, the thermal and shot noise-limited detectivity of the SML QD-QCD is calculated as follows [31]:

$$D^* = \frac{R\sqrt{A}}{\sqrt{i_{total}^2/B}} \quad (5)$$

here R is the peak responsivity, A is the device area, B is the bandwidth and i_{total} is the device total noise which can be extracted from Fig. 10. The calculated D^* of the SML QD-QCD device at 77 K, 90 K and 100 K are shown in Fig. 11. The

peak D^* at 100 K is $6.6 \times 10^7 \text{ cm} \cdot \text{Hz}^{1/2}/\text{W}$, and it increases to

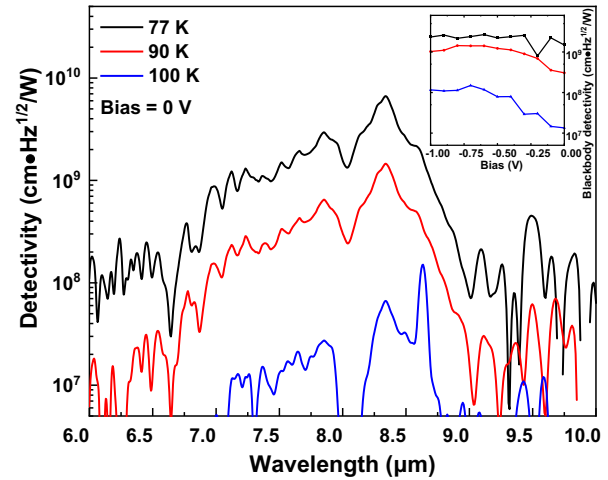


Fig. 11. The calculated detectivity of the SML QD-QCD device measured at 77 K, 90 K and 100 K under zero bias. The inset plots the blackbody detectivity versus reverse bias.

$6.5 \times 10^9 \text{ cm} \cdot \text{Hz}^{1/2}/\text{W}$ when temperature lowers to 77 K. The inset of Fig. 11 shows the blackbody detectivity as a function of reverse bias. The detectivity increases with increasing bias, due to the larger enhancement in responsivity than noise as already demonstrated in Fig. 9 and 10. Compared with the LWIR QCD based on quantum dash and with a cutoff wavelength $\sim 10 \mu\text{m}$ ($D^* \sim 2 \times 10^8 \text{ cm} \cdot \text{Hz}^{1/2}/\text{W}$ at 77 K, 0 V), in spite of a comparable responsivity, our device shows an order of magnitude higher detectivity, thanks to the relative lower noise [32]. However, compared with recently reported patch antenna QW-QCD targeted at $9 \mu\text{m}$ with a zero-bias responsivity of $50 \text{ mA}/\text{W}$ at room temperature ($D^* \sim 1 \times 10^{10} \text{ cm} \cdot \text{Hz}^{1/2}/\text{W}$ at 77 K, 0 V) [9], the detectivity of our device is half a magnitude smaller due to lower responsivity. It is worth noting that different than the traditional QDIP devices which rely on external electric field, in QCD design the photo-generated carriers are extracted by phonon-assisted cascade transport, and hence zero-bias operation and low dark current noise are achieved at the cost of the quantum efficiency (QE) of the device. Thus, in order to further boost the detectivity while still enjoying the merit of zero-bias operation, optimization of the present SML QD-QCD device should be directed towards the enhancement of QE and reduction of noise. The device QE (i.e., absorption strength) is related to the electron wavefunction overlapping in the SML QD active region, which can be further improved by careful redesign of SML QD layer thickness and stack number to increase the vertical coupling of QDs. On the other hand, the noise of the device can be improved by using more resonant tunneling layer for carrier transport.

V. CONCLUSION

In summary, a normal incident long-wave infrared quantum cascade photodetector based on sub-monolayer InAs/GaAs quantum dots has been demonstrated and characterized. Optical properties of the SML QD active region have been studied by temperature- and excitation-dependent PL, which reveal a mixed QD-QW ground state due possibly to the atomic inter-diffusion of In-Ga at the InAs/(In)GaAs interface.

The device exhibits two main photoresponse peaks at 7.6 and 8.3 μm , with a peak responsivity of 7.5 mA/W observed at 8.3 μm at 77 K and under zero bias. The corresponding thermal and shot noise-limited detectivity is $6.5 \times 10^9 \text{ cm} \cdot \text{Hz}^{1/2} / \text{W}$. These optical and device performance characteristics pave the way for the application of this SML QD-QCD as a competitive candidate for fabricating long-wave infrared focal plane arrays with very low power dissipation. The device performance can be further improved through enhancing the device quantum efficiency and reducing the current noise by fine-tuning the SML QD stack thickness and the number of carrier extracting quantum wells.

REFERENCES

- [1] K. Sujka and P. Koczoń, "The application of FT-IR spectroscopy in discrimination of differently originated and aged whisky," *European Food Research and Technology*, vol. 244, no. 11, pp. 2019-2025, 2018, doi: 10.1007/s00217-018-3113-5.
- [2] A. Rogalski, J. Antoszewski, and L. Faraone, "Third-generation infrared photodetector arrays," *Journal of Applied Physics*, vol. 105, no. 9, 2009, doi: 10.1063/1.3099572.
- [3] A. F. Goetz, G. Vane, J. E. Solomon, and B. N. Rock, "Imaging spectrometry for Earth remote sensing," *Science*, vol. 228, no. 4704, pp. 1147-53, Jun 7 1985, doi: 10.1126/science.228.4704.1147.
- [4] P. Hellwig and F. Melin, *Recent Applications of Infrared Spectroscopy and Microscopy in Chemistry, Biology and Medicine*. 2010.
- [5] L. Gendron, M. Carras, A. Huynh, V. Ortiz, C. Koeniguer, and V. Berger, "Quantum cascade photodetector," *Applied Physics Letters*, vol. 85, no. 14, pp. 2824-2826, 2004, doi: 10.1063/1.1781731.
- [6] D. Hofstetter, M. Beck, and J. Faist, "Quantum-cascade-laser structures as photodetectors," *Applied Physics Letters*, vol. 81, no. 15, pp. 2683-2685, 2002, doi: 10.1063/1.1512954.
- [7] F. R. Giorgetta, E. Baumann, M. Graf, Q. Yang, C. Manz, K. Kohler, H. E. Beere, D. A. Ritchie, E. Linfield, A. G. Davies, Y. Fedoryshyn, H. Jackel, M. Fischer, J. Faist, and D. Hofstetter, "Quantum Cascade Detectors," *IEEE Journal of Quantum Electronics*, vol. 45, no. 8, pp. 1039-1052, 2009, doi: 10.1109/jqe.2009.2017929.
- [8] J. Liu, Y. Zhou, S. Zhai, F. Liu, S. Liu, J. Zhang, N. Zhuo, L. Wang, and Z. Wang, "High-frequency very long wave infrared quantum cascade detectors," *Semiconductor Science and Technology*, vol. 33, no. 12, 2018, doi: 10.1088/1361-6641/aaebd4.
- [9] A. Bigioli, G. Armaroli, A. Vasanelli, D. Gacemi, Y. Todorov, D. Palaferri, L. Li, A. G. Davies, E. H. Linfield, and C. Sirtori, "Long-wavelength infrared photovoltaic heterodyne receivers using patch-antenna quantum cascade detectors," *Applied Physics Letters*, vol. 116, no. 16, 2020, doi: 10.1063/5.0004591.
- [10] J. Huang, Y. Wan, D. Jung, J. Norman, C. Shang, Q. Li, K. M. Lau, A. C. Gossard, J. E. Bowers, and B. Chen, "Defect Characterization of InAs/InGaAs Quantum Dot p-i-n Photodetector Grown on GaAs-on-V-Grooved-Si Substrate," *ACS Photonics*, vol. 6, no. 5, pp. 1100-1105, April 23, 2019, doi: 10.1021/acsp Photonics.8b01707.
- [11] B. Chen, Y. Wan, Z. Xie, J. Huang, N. Zhang, C. Shang, J. Norman, Q. Li, Y. Tong, and K. M. Lau, "Low dark current high gain InAs quantum dot avalanche photodetectors monolithically grown on Si," *ACS Photonics*, vol. 7, no. 2, pp. 519-527, 2020, doi: 10.1021/acsp Photonics.9b01648.
- [12] S. Chen, W. Li, J. Wu, Q. Jiang, M. Tang, S. Shutts, S. N. Elliott, A. Sobiesierski, A. J. Seeds, and I. Ross, "Electrically pumped continuous-wave III-V quantum dot lasers on silicon," *Nature Photonics*, vol. 10, no. 5, p. 307, 2016.
- [13] A. V. Barve and S. Krishna, "Photovoltaic quantum dot quantum cascade infrared photodetector," *Applied Physics Letters*, vol. 100, no. 2, 2012, doi: 10.1063/1.3675905.
- [14] X.-J. Wang, S.-Q. Zhai, N. Zhuo, J.-Q. Liu, F.-Q. Liu, S.-M. Liu, and Z.-G. Wang, "Quantum dot quantum cascade infrared photodetector," *Applied Physics Letters*, vol. 104, no. 17, 2014, doi: 10.1063/1.4874802.
- [15] J. Huang, D. Guo, Z. Deng, W. Chen, H. Liu, J. Wu, and B. Chen, "Midwave Infrared Quantum Dot Quantum Cascade Photodetector Monolithically Grown on Silicon Substrate," *Journal of Lightwave Technology*, vol. 36, no. 18, pp. 4033-4038, 2018.
- [16] J. Huang, D. Guo, W. Chen, Z. Deng, Y. Bai, T. Wu, Y. Chen, H. Liu, J. Wu, and B. Chen, "Sub-monolayer quantum dot quantum cascade mid-infrared photodetector," *Applied Physics Letters*, vol. 111, no. 25, 2017, doi: 10.1063/1.5011239.
- [17] D. Z.-Y. Ting, S. V. Bandara, S. D. Gunapala, J. M. Mumolo, S. A. Keo, C. J. Hill, J. K. Liu, E. R. Blazewski, S. B. Rafol, and Y.-C. Chang, "Submonolayer quantum dot infrared photodetector," *Applied Physics Letters*, vol. 94, no. 11, p. 111107, 2009.
- [18] B. Chen, "Active Region Design and Gain Characteristics of InP-Based Dilute Bismide Type-II Quantum Wells for Mid-IR Lasers," *IEEE Transactions on Electron Devices*, vol. 64, no. 4, pp. 1606-1611, 2017.
- [19] B. Chen, W. Jiang, and A. Holmes Jr, "Design of strain compensated InGaAs/GaAsSb type-II quantum well structures for mid-infrared photodiodes," *Optical and Quantum Electronics*, vol. 44, no. 3, pp. 103-109, 2012.
- [20] B. Chen, "Optical gain analysis of GaAs-based InGaAs/GaAsSbBi type-II quantum wells lasers," *Optics Express*, vol. 25, no. 21, pp. 25183-25192, 2017.
- [21] B. Chen and A. Holmes Jr, "Optical gain modeling of InP based InGaAs (N)/GaAsSb type-II quantum wells laser for mid-infrared emission," *Optical and Quantum Electronics*, vol. 45, no. 2, pp. 127-134, 2013.
- [22] Z. Deng, B. Chen, X. Chen, J. Shao, Q. Gong, H. Liu, and J. Wu, "Optical properties of beryllium-doped GaSb epilayers grown on GaAs substrate," *Infrared Physics & Technology*, vol. 90, pp. 115-121, 2018, doi: 10.1016/j.infrared.2018.03.004.
- [23] D. Orani, A. Polimeni, A. Patané, M. Capizzi, F. Martelli, A. D'Andrea, N. Tomassini, P. Borri, M. Gurioli, and M. Colocci, "Binding Energy and Lifetime of Excitons in InxGa1-xAs/GaAs Quantum Wells," *physica status solidi (a)*, vol. 164, pp. 107-110, 11/01 1997, doi: 10.1002/1521-396X(199711)164:1<107::AID-PSSA107>3.0.CO;2-8.
- [24] G. Wang, S. Fafard, D. Leonard, J. Bowers, J. Merz, and P. Petroff, "Time-resolved optical characterization of InGaAs/GaAs quantum dots," *Applied Physics Letters*, vol. 64, pp. 2815-2817, 06/01 1994, doi: 10.1063/1.111434.
- [25] N. Georgiev and T. J. J. o. A. P. Mozume, "Photoluminescence study of InGaAs/AlAsSb heterostructure," vol. 89, no. 2, p. 1064, 2001.
- [26] Z. Deng, D. Guo, C. González Burguete, Z. Xie, J. Huang, H. Liu, J. Wu, and B. Chen, "Demonstration of Si based InAs/GaSb type-II superlattice p-i-n photodetector," *Infrared Physics & Technology*, vol. 101, 06/01 2019, doi: 10.1016/j.infrared.2019.06.011.
- [27] T. Schmidt, K. Lischka, and W. Zulehner, "Excitation-power dependence of the near-band-edge photoluminescence of semiconductors," *Physical review. B, Condensed matter*, vol. 45, pp. 8989-8994, 05/01 1992, doi: 10.1103/PhysRevB.45.8989.
- [28] Z. Xu, K. Leosson, D. Birkedal, V. Lyssenko, J. r. M. Hvam, and J. J. N. Sadowski, "InGaAs/GaAs quantum-dot-quantum-well heterostructure formed by submonolayer deposition," vol. 14, no. 12, pp. 1259-1261.
- [29] W. Chen, Z. Deng, D. Guo, Y. Chen, Y. I. Mazur, Y. Maidaniuk, M. Benamara, G. J. Salamo, H. Liu, J. Wu, and B. Chen, "Demonstration of InAs/InGaAs/GaAs Quantum Dots-in-a-Well Mid-Wave Infrared Photodetectors Grown on Silicon Substrate," *Journal of Lightwave Technology*, vol. 36, no. 13, pp. 2572-2581, 2018, doi: 10.1109/JLT.2018.2811388.
- [30] I. S. Han, J. S. Kim, J. C. Shin, J. O. Kim, S. K. Noh, S. J. Lee, and S. Krishna, "Photoluminescence study of InAs/InGaAs submonolayer quantum dot infrared photodetectors with various numbers of multiple stack layers," *Journal of Luminescence*, vol. 207, pp. 512-519, 2019, doi: 10.1016/j.jlum.2018.11.052.
- [31] Lu, Armiento, Li, and Goodhue, "A Longwave Infrared (LWIR) Photodetector Based on Nonlinear Absorption in InAs/GaAs Quantum Dots," in *International Symposium on Biophotonics*, 2006.
- [32] F.-J. Wang, F. Ren, S.-M. Liu, N. Zhuo, S.-Q. Zhai, J.-Q. Liu, F.-Q. Liu, and Z.-G. Wang, "Normal incident long wave infrared quantum dash quantum cascade photodetector," *Nanoscale research letters*, vol. 11, no. 1, p. 392, 2016.